Geophysical Research Letters

RESEARCH LETTER
10.1029/2025GL116054

Mantle Flow and Fault Zone Related Seismic Anisotropy Revealed by a Dense Linear Broadband Array in Southeast Tibet

Jing Wu[1], Yinshuang Ai[2], Stephen S. Gao[3], Peixi Huang[1], Fansheng Kong[4], Deke Xu[1], Jianguo Song[5], Xinyu Gao[1], Mengyi Wei[1], Long Li[6], Jien Zhang[1], Yanbin Zhang[1], and Yingying Zhang[7]

[1]State Key Laboratory of Lithospheric and Environmental Coevolution, Institute of Geology and Geophysics, Chinese Academy of Sciences, Beijing, China, [2]Key Laboratory of Earth and Planetary Physics, Institute of Geology and Geophysics, Chinese Academy of Sciences, Beijing, China, [3]Department of Earth Sciences and Engineering, Missouri University of Science and Technology, Rolla, MO, USA, [4]State Key Laboratory of Submarine Geoscience, Hangzhou, China, [5]China University of Petroleum - East China, Qingdao, China, [6]Beijing Earthquake Agency, Beijing, China, [7]China Earthquake Networks Center, Beijing, China

Abstract Southeast Tibet, a key region for the southeastward extrusion of the Tibetan Plateau, remains debated in terms of its tectonic deformation in response to the ongoing collision between the Indian and Eurasian plates. In this study, we applied shear-wave splitting analysis of core-refracted phases recorded by a newly deployed dense seismic array and six permanent stations to delineate crustal and mantle deformation processes. The observed fast polarization directions are predominantly aligned NNW–SSE, while the splitting delay times vary across four sub-blocks. The anisotropy pattern suggests a dominantly asthenospheric origin, consistent with southeastward-directed mantle flow associated with the extrusion of the Tibetan lithosphere. The splitting delay times are relatively larger near major faults and tectonic boundaries compared to areas farther away, and the fast polarization directions beneath these structures exhibit a moderate rotation toward the fault strike, indicating that such tectonic discontinuities contribute to observable azimuthal anisotropy.

Plain Language Summary The Tibetan Plateau is one of the most tectonically active regions on Earth, with southeast Tibet acting as a key area accommodating the plateau's southeastward expansion. However, how the crust and mantle beneath this region deform in response to the ongoing collision between the Indian and Eurasian plates remains a topic of debate, particularly in regions where multiple large-scale faults intersect. In this study, we used shear-wave splitting, a seismic method similar to optical birefringence, to analyze data from a new dense seismic array and six permanent stations in southeast Tibet. We found that fast polarization directions are mostly aligned in the NNW–SSE direction and likely originate from the asthenosphere, indicating southeastward mantle flow. Importantly, the splitting delay times are larger near major faults and tectonic boundaries, and the fast directions rotate moderately toward the fault strike, suggesting that these structures influence seismic anisotropy. Although previous studies have proposed low-velocity layers beneath the region, our results show no clear correlation between these layers and the anisotropy parameters. Our findings highlight that large-scale faults in southeast Tibet are mostly confined in the crust and may play a significant role in controlling the observed seismic anisotropy.

Key Points:

- Data from a dense linear broadband seismic array yields high resolution shear wave splitting data in Southeast Tibet
- Fast polarization directions align NNW–SSE, indicating southeastward asthenospheric mantle flow
- Fault zones rotate fast directions and produce delay-time steps, corresponding to fault penetration depths of 9–26 km

Supporting Information:

Supporting Information may be found in the online version of this article.

Correspondence to:

J. Wu,
wujing_js@mail.iggcas.ac.cn

Citation:

Wu, J., Ai, Y., Gao, S. S., Huang, P., Kong, F., Xu, D., et al. (2025). Mantle flow and fault zone related seismic anisotropy revealed by a dense linear broadband array in southeast Tibet. *Geophysical Research Letters*, *52*, e2025GL116054. https://doi.org/10.1029/2025GL116054

Received 25 MAR 2025
Accepted 3 AUG 2025

Author Contributions:

Conceptualization: Jing Wu
Data curation: Yinshuang Ai, Stephen S. Gao, Peixi Huang, Fansheng Kong, Xinyu Gao, Mengyi Wei, Long Li, Yingying Zhang
Formal analysis: Jing Wu
Funding acquisition: Jing Wu, Yinshuang Ai, Deke Xu, Jianguo Song
Methodology: Jing Wu
Project administration: Jing Wu, Yinshuang Ai
Resources: Yinshuang Ai
Visualization: Peixi Huang, Xinyu Gao, Mengyi Wei, Jien Zhang, Yanbin Zhang
Writing – original draft: Jing Wu

1. Introduction

The Tibetan Plateau, often referred to as the "third pole" of the world, is distinguished by intense crustal and mantle deformation resulting from the ongoing collision between the Indian and Eurasian plates since approximately 70 Ma (Yin & Harrison, 2000). Three primary geodynamic models have been proposed to explain the evolution of the largest continental plateau on Earth: tectonic escape (Tapponnier et al., 2001), lower crustal flow (Clark & Royden, 2000), and crustal shortening (Hubbard & Shaw, 2009). Southeast Tibet, characterized by frequent large earthquakes and the intersection of multiple major fault systems, serves as a key pathway for the southeastward extrusion of the plateau (Figure 1a). Various geodynamic models have been proposed to explain crustal deformation in southeast Tibet. Some researchers have suggested the presence of large-scale lower crustal flow (Bai et al., 2010), while others argue against its existence (Hu et al., 2022) or propose that only localized crustal flow is likely (Bao et al., 2020). Based on a decade of observations from permanent seismic stations and

10.1029/2025GL116054

Writing – review & editing: Jing Wu, Stephen S. Gao, Fansheng Kong

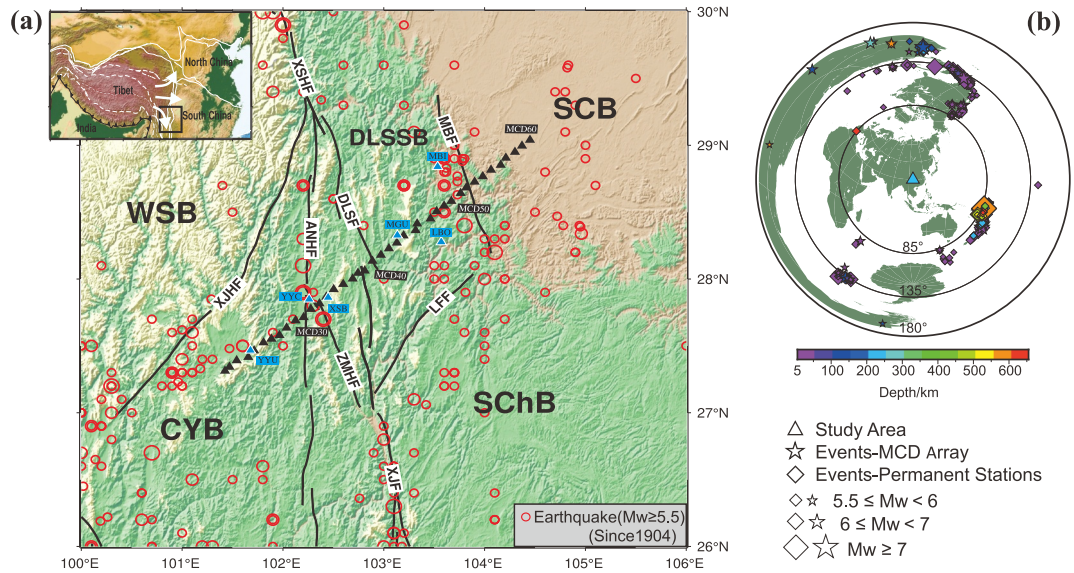

Figure 1. (a) Tectonics, faults, earthquakes, and seismic stations in the study area. WSB: West Sichuan block, CYB: Central Yunnan block, SCB: Sichuan basin, SChB: South China block, DLSSB: Daliangshan sub-block, XJHF: Xiaojinhe fault, XSHF: Xianshuihe fault, ANHF: Anninghe fault, ZMHF: Zemuhe fault, XJF: Xiaojiang fault, LFF: Lianfeng fault, DLSF: Daliangshan fault, and MBF: Mabian fault. Red circles indicate earthquakes with Mw ≥ 5 since 1904, black triangles are stations in the Middle ChuanDian (MCD) array, while blue triangles are permanent stations with their names labeled. The inset at the left-upper corner shows the Tibetan Plateau and adjacent areas, in which arrows show the eastward expansion of the Tibetan Plateau, and the rectangle marks the study area. (b) Spatial distribution of events used in this study. Events used in the MCD array are marked by stars, while events used in permanent stations are represented by diamonds. The depths of the seismic events are color coded.

crustal anisotropy derived from Pms arrival times, recent studies further suggest that both major fault systems and localized crustal flow may play significant roles in accommodating crustal deformation in this region (P. Huang et al., 2024). Given the presence of several prominent strike-slip faults, including the Anninghe–Zemuhe Fault (ANHF–ZMHF), Daliangshan Fault (DLSF), and Mabian Fault (MBF), it remains an open question whether these structures exert primary control on crustal and lithospheric deformation beneath southeast Tibet. However, efforts to resolve this question are hindered by the sparse spatial distribution of permanent seismic stations, particularly near these major fault zones (Figure 1a).

Seismic anisotropy refers to the directional dependence of seismic velocity, amplitude, and other physical properties. Major causes of seismic anisotropy include lattice preferred orientation and shape preferred orientation (Long & Silver, 2009; S. Zhang & Karato, 1995). Observations show that seismic anisotropy exists broadly in the Earth (Crampin & Peacock, 2005; Savage, 1999; Silver, 1996; Vinnik et al., 1989). Multiple methods can be applied to invert seismic anisotropy, including body wave anisotropic tomography (J. Wang et al., 2019; D. Zhao et al., 2023), surface wave anisotropic tomography (Montagner & Nataf, 1986), and shear-wave splitting (Crampin, 1984; Silver & Chan, 1991), among which shear-wave splitting has the advantage of high horizontal resolution, which is especially important to discriminate fault zone related deformation.

Shear-wave splitting is typically characterized by two physical parameters, the polarization of the fast shear-wave (φ), and the delay time of the slow shear-wave (δt). In theory, multiple shear-wave phases traveling through various layers in the Earth could be used. For example, S splitting from local events may show middle-upper crustal anisotropy beneath continents (Crampin & Peacock, 2005; Teanby et al., 2004), XKS (mainly including SKS, SKKS, and PKS) splitting from distant events ($\Delta \geq 85°$) could reveal lithospheric/asthenospheric anisotropy (McNamara et al., 1994; Silver & Chan, 1991; L. Zhao et al., 2014), while the time moveout of the Moho-transformed Ps phase (Pms: $\Delta = 30°–90°$) may unravel whole-crustal deformation (H. Liu & Niu, 2012; Rümpker et al., 2014). In this study, we focus on southeast Tibet, a region marked by multiple large-scale faults, to investigate the characteristics of mantle flow and the role of fault zones in lithospheric deformation. This analysis is based on XKS shear-wave splitting measurements obtained from the Middle ChuanDian (MCD) array, a dense linear broadband seismic network that crosses several major fault systems.

2. Data and Method

The linear MCD array, approximately 500 km in length and oriented from southwest to northeast, was deployed by the Institute of Geology and Geophysics, Chinese Academy of Sciences from December 2018 to October 2020. It crosses several major faults, including the ANHF, ZMHF, DLSF, and MBF. The MCD array consists of 40 broadband seismic stations (labeled MCD21–MCD60, Figure 1a), equipped with 17 Trillium Posthole and 23 Trillium Horizon 120 sensors, each recording at a sampling rate of 100 Hz. The stations are spaced at an average interval of approximately 10 km (F. Yang et al., 2023).

As demonstrated by previous studies (e.g., Wu et al., 2015), 2 years of observation from a temporary array such as MCD are generally sufficient for XKS splitting analysis. However, incorporating long-term data from nearby permanent stations would enhance the reliability assessment of the MCD measurements and help verify their robustness. Thus, we downloaded waveforms from six permanent stations around MCD from the Data Management Centre of the China National Seismic Network, Institute of Geophysics, China Earthquake Administration. The stations (YYC, YYU, XSB, LBO, MBI, and MGU) are equipped with BBVAS60 or KS2000 broadband seismometers and operate at a 100 Hz sampling rate, providing approximately 13 years of continuous seismic observations from January 2010 to October 2022 (Figure 1a).

We selected events with epicentral distances of 85°–180° and Mw ≥ 5.5, based on the NEIC catalog (https://earthquake.usgs.gov/earthquakes/search/). Next, we applied three types of bandpass filters to the horizontal components in 0.02–0.3, 0.01–0.4, and 0.04–0.5 Hz, ensuring the inclusion of the main XKS energy (Favier & Chevrot, 2003). Finally, a total of 68 events are available for shear-wave splitting analysis of data from the MCD array, and 481 events are available for the permanent stations. These events are mainly located in the Fiji-Tonga and South American subduction zones (Figure 1b). Most of the core-refracted phases used in this study are PKS, SKS, and SKKS (1,557 non-null measurements), in addition to 25 measurements from sSKS and pSKS.

Among multiple anisotropy analysis methods, shear-wave splitting has a significant advantage in measuring fine-scale anisotropic structures with high horizontal resolution (X. Zhao & Wu, 2024). In this study, single-event analysis methods were utilized to measure seismic anisotropic parameters by using SplitLab (Wüstefeld et al., 2008), which integrates the rotation-correlation method (RC, Bowman & Ando, 1987), the minimum energy method (SC, Silver & Chan, 1991) and the eigenvalue method (EV, Silver & Chan, 1991). To ensure the quality of the analysis, only waveforms with a signal-to-noise (SNR) ≥ 4 are retained (Restivo & Helffrich, 1999). Although we computed XKS splitting parameters using all three methods, quality assessments were based primarily on the results from the RC and SC methods, which are generally considered more robust. Figure 2 shows the analysis examples of events recorded by different stations from various back-azimuths.

3. Results

3.1. Quality Assessment

Quality assessment is important in XKS splitting analysis, and this is especially true for the single event method. In general, the differences between the parameter pair (φ, δt) estimated by the RC and the SC can be used to assess the quality of the splitting measurements (Wüstefeld & Bokelmann, 2007). First, we define parameters $\rho = \delta t_{RC}/\delta t_{SC}$ and $\Phi = |\varphi_{RC} - \varphi_{SC}|$, following criterions of Wüstefeld and Bokelmann (2007). When $0.7 \leq \rho \leq 1.1$ and $\Phi \leq 12°$, the individual measurement is assessed as "good," while when $0.6 \leq \rho \leq 1.2$ and $\Phi \leq 18°$, it is assessed as "fair." Additionally, when $\rho \leq 0.25$ and $35° \leq \Phi \leq 55°$, the measurement is a "null," meaning weak anisotropy or that the initial polarization of the incident shear-wave is parallel or perpendicular to the back azimuth of the event.

Next, in addition to the criterion mentioned above, we also applied the following qualitative criteria through visual checking (X. Chen et al., 2018): (a) The size and shape of the shadow in error plane, (b) Particle motion before and after seismic anisotropy correction, (c) The robustness of the measurement under the conditions with different filters and time windows, and (d) The consistency of the results obtained by the two methods (the RC and the SC). Therefore, in addition to $0.7 \leq \rho \leq 1.1$ and $\Phi \leq 12°$, a good shear-wave splitting case should also exhibit the following characteristics: a well-defined error surface, elliptical particle motion before anisotropy correction that becomes linear afterward, and consistent splitting parameters across different time windows and bandpass filter settings. Finally, we obtained 1,278 good measurements and 279 fair measurements (Table S1). In addition, 320 null measurements from the MCD array were identified (Table S1, Figures S1–S3 in

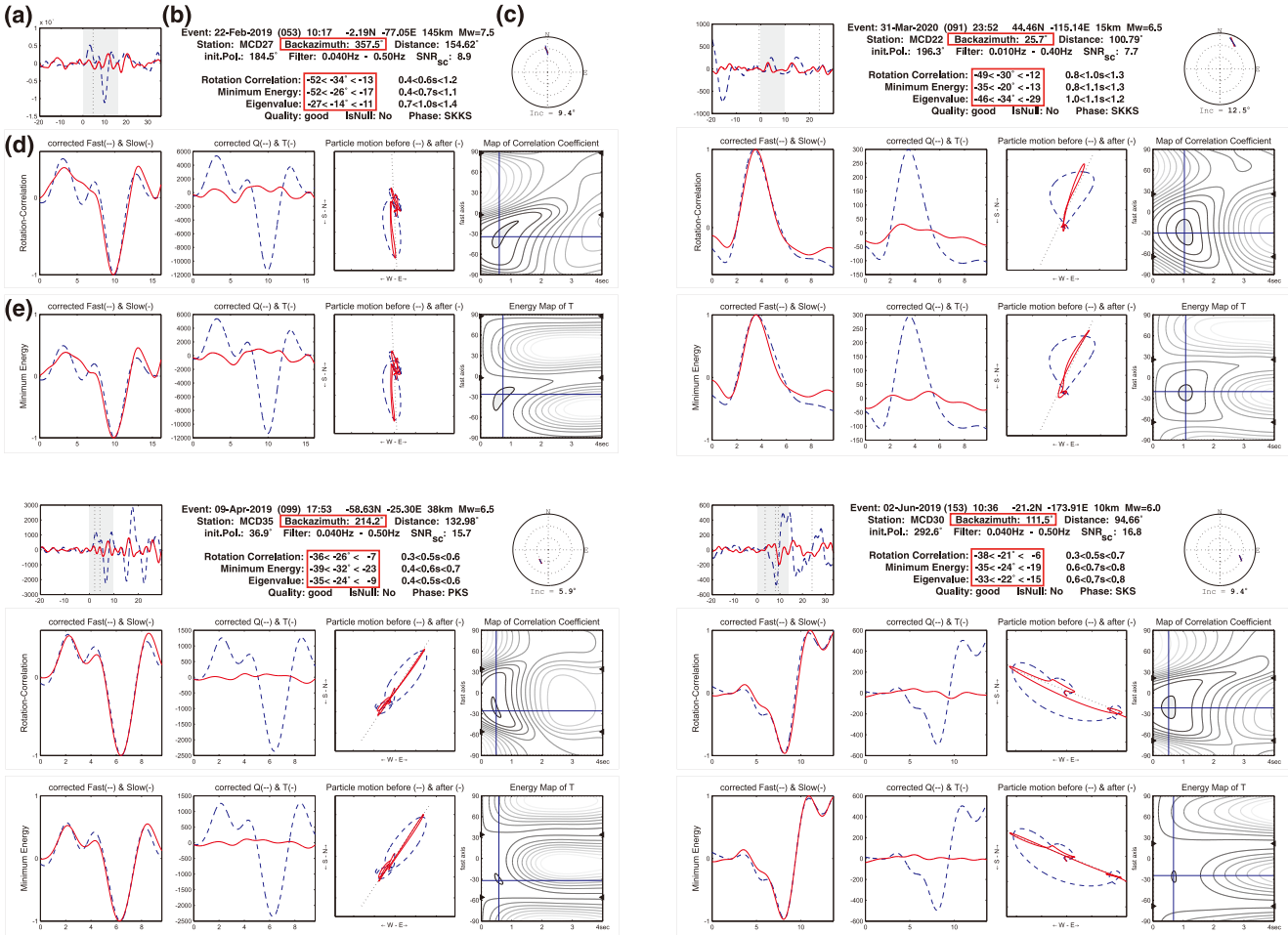

Figure 2. XKS splitting parameters of four events from different back-azimuths. For each event: (a) Original radial (in blue) and transverse (in red) components of the XKS arrival. (b) Major information related to the measurement. (c) Back azimuth (black bar) of the event. (d) Analysis processes with the method of Rotation Correlation, from left to right column: fast and slow waveforms after seismic anisotropy correction, radial and transverse components after seismic anisotropy correction, particle motion before (in blue) and after (in red) correction, and optimal fitting of the shear-wave splitting parameters. (e) Same as (d), but for the method of Minimum Energy.

Supporting Information S1 for good/fair/null ones). The measurements include 25 sSKS or pSKS measurements, which are from deep-focus earthquakes with depths ≥150 km and magnitudes Mw ≥ 6.0. Among them, 23 events originate from depths greater than 300 km, ensuring effective separation of deep-focal phases from other seismic phases. Additionally, no outliers in splitting parameters are observed for sSKS and pSKS when compared to typical XKS phases (Figure S4 in Supporting Information S1). In the following discussion, we primarily focus on measurements classified as "good" or "fair."

3.2. Consistency of XKS Splitting Parameters From the MCD Array and the Permanent Stations

Of the 40 stations in the MCD array, 32 have at least five reliable measurements (further discussed in the following sections), while all six permanent stations have more than five reliable measurements as well (Table S2). Figure S5 in Supporting Information S1 shows rose diagrams of fast polarization directions for both the MCD array (blue for stations with more than five reliable measurements and black for those with fewer) and the permanent stations (red). The results reveal a consistent NNW–SSE orientation of fast polarizations. Additionally, the delay times observed at the MCD stations closely match those at nearby permanent stations (Figures 3 and 4). The consistency suggests that reliable splitting measurements can be obtained at portable stations with an approximately 2-year duration of deployment.

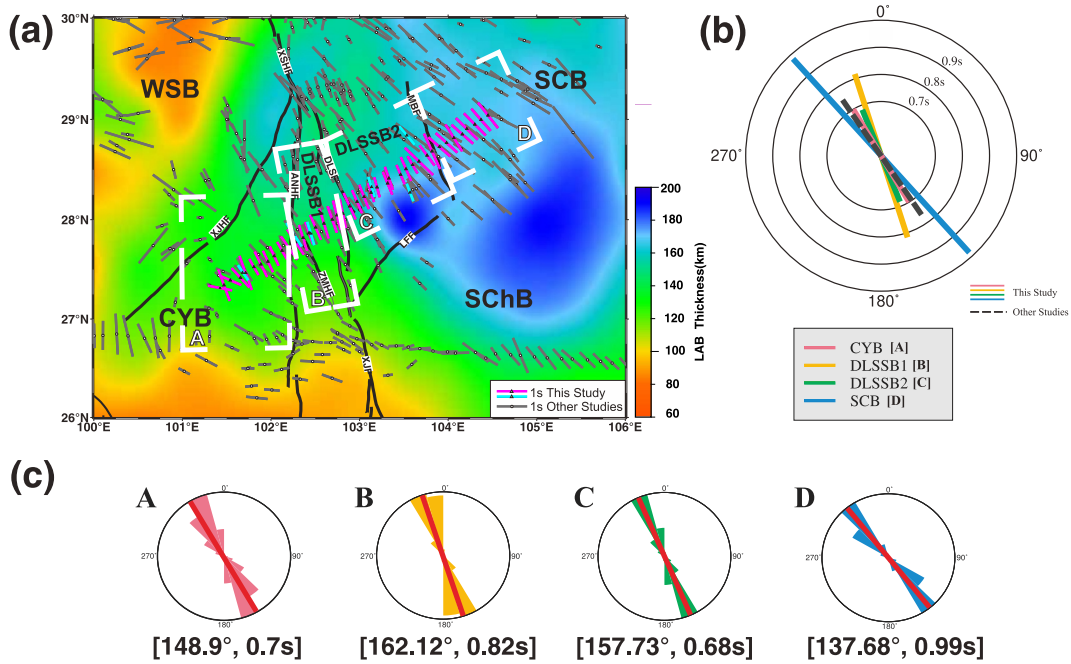

Figure 3. Results of XKS splitting analysis. (a) XKS splitting parameters plotted on lithospheric thickness (A. Zhang et al., 2024). The short bars are fast polarization directions, with the length being proportional to the delay time. Red bars: measurements from the Middle ChuanDian array, Blue bars: measurements from permanent stations, and Gray bars: results from previous studies (W. Li et al., 2021; J. Liu et al., 2020; C. Y. Wang et al., 2008; Y. Yang et al., 2018). White rectangles mark four sub-areas (A to D). DLSSB1: Daliangshan sub-block 1 and DLSSB2: Daliangshan sub-block 2. Other symbols are the same as those in Figure 1. (b) Average splitting parameters for the four sub-areas, plotted in different colors. The black dashed bar shows the average value from previous studies. (c) Rose diagrams showing the splitting parameters for each sub-area. The average fast polarization and delay time are shown at the bottom of each rose diagram.

3.3. Spatial Distribution of XKS Splitting Parameters

To observe the variation in delay time along the profile, we divided it into four sub-blocks, labeled A to D from southwest to northeast, including CYB (Central Yunnan Block), DLSSB1 (Daliangshan Sub Block 1), DLSSB2 (Daliangshan Sub Block 2), and Sichuan Basin (SCB), by considering both the tectonics and delay time discrepancies (Figure 3a). Owing to the dense station spacing (~10 km) of the MCD array, this study reveals a number of detailed patterns of seismic anisotropy. First, as shown in Figure 3a, a prominent consistency in fast polarization directions, predominantly oriented NNW–SSE, is observed along the MCD array (indicated by red bars), closely matching the results from previous studies (shown in gray bars). Second, the influence of major faults on the observed splitting is evident from localized alignments of fast polarization directions with fault strikes, most notably near the MBF Belt (MFB) and the Daliangshan Fault (DLSF). Third, within the SCB, the fast polarizations tend to shift toward a more east–west orientation. Fourth, for some of the stations with good azimuthal coverages (YYC, YYU, and MBI), the fast polarizations for events from the north have a larger departure from the N-S direction relative to fast polarizations of events from other azimuths (Figures S6 and S7 in Supporting Information S1).

Furthermore, the average delay times are relatively larger beneath DLSSB1 (0.82 ± 0.21 s) and the SCB (0.99 ± 0.23 s), both of which are located near major fault zones. In contrast, smaller delay times are observed beneath the CYB (0.70 ± 0.32 s) and DLSSB2 (0.68 ± 0.16 s), where the stations are farther from active faults (Figures 3b and 3c). Notably, Block C exhibits the smallest average delay time compared to Blocks B and D, with localized increases in delay times near fault zones (Figures 3a and 4c–4d). Overall, the mean delay time across all measurements is 0.83 ± 0.18 s (Table S3), which is lower than the global average of approximately 1.0 s for continents (Silver, 1996).

To evaluate whether the relatively small and spatially varying delay times are due to frequency dependence, we examined two permanent stations located in DLSSB2, including LBO (with 285 measurements) and MBI (with

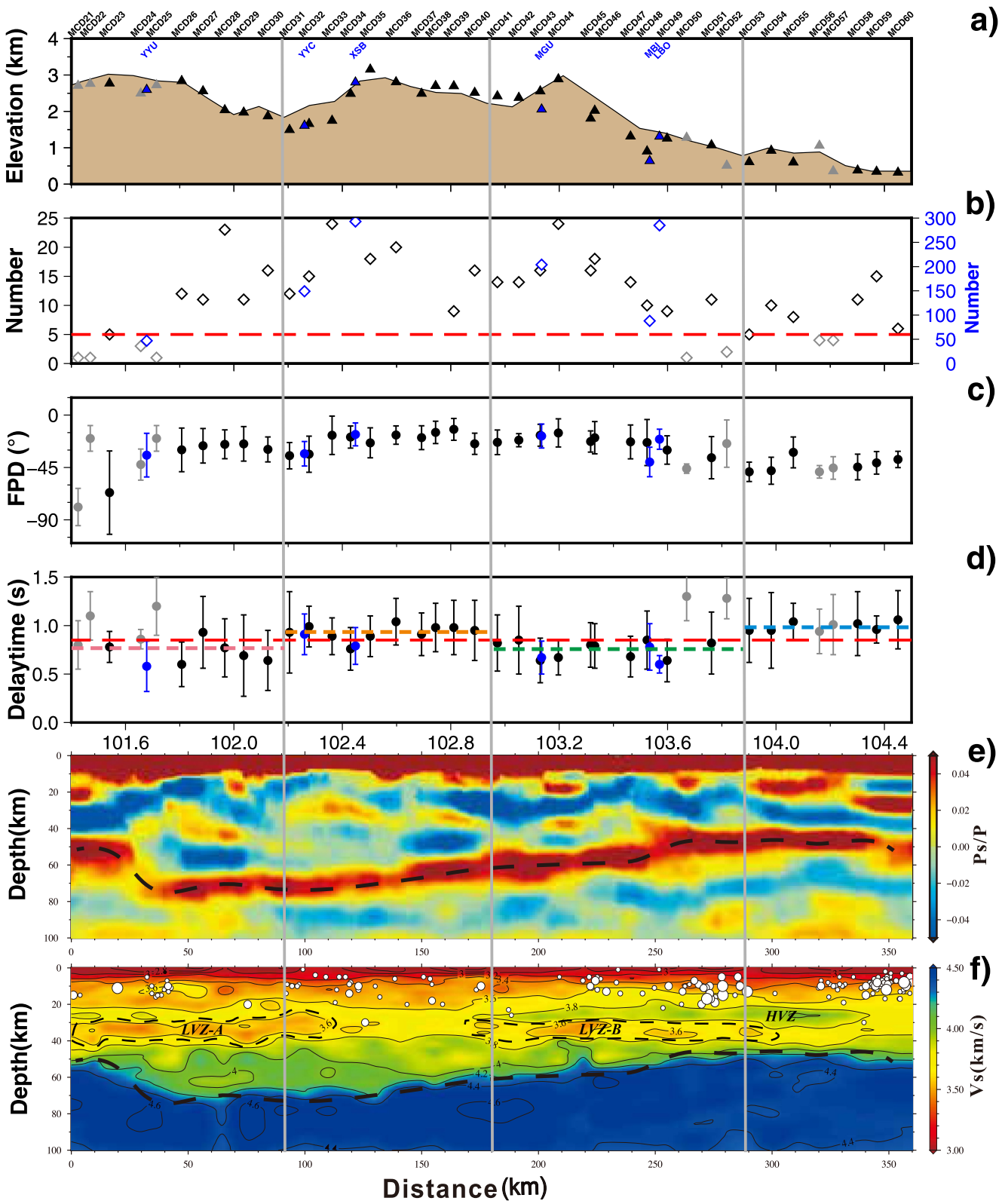

Figure 4.

88 measurements), which exhibit the smallest average delay times. For each station, we extracted the XKS phases using a time window from −20 to +30 s relative to the XKS arrival times and computed the dominant frequencies of the two horizontal components using the Fast Fourier Transform. We then plotted the dominant frequency against delay time (Figure S8 in Supporting Information S1). The results show that, for both stations, the delay times are independent of the dominant frequency, indicating that the observed variations in delay time are more likely spatially controlled by tectonic structure rather than frequency-dependent effects.

4. Discussion

Totally, we obtained 1,877 pairs of shear-wave splitting parameters with quality "good," "fair," and "null." In addition, with a few exceptions which will be discussed below, events coming from different back-azimuths show similar fast polarization directions and delay times (Figure 2 and Figure S5 in Supporting Information S1), suggesting the presence of a single-layer anisotropy with a horizontal symmetry axis beneath southeast Tibet, an observation that aligns well with previous studies (W. Li et al., 2021; J. Liu et al., 2020; C. Y. Wang et al., 2008; Y. Yang et al., 2018). The new splitting measurements from the dense array offer valuable insights into the underlying mantle flow field and highlight the influence of major fault zones and tectonic boundaries in shaping the observed azimuthal anisotropy.

4.1. Comparison With Previous Azimuthal Anisotropy Studies

Previous studies suggest that local S splitting, which is mostly related to anisotropy in the seismogenic upper-mid crust, around the MCD array is predominantly NNW–SSE, parallel to stress or fault-zone strikes, with delay times of 0.02–0.07 s (Figures S9a and S9d in Supporting Information S1, Table S3; A. Chen et al., 2019; Y. Zhang & Gao, 2017). On the other hand, Pms-derived anisotropy, which measures anisotropy of the entire crust, is more scattered. For example, dual predominant polarizations beneath CYB and DLSSB2 with delays of 0.24–0.53 s are observed (Figures S9b and S9d in Supporting Information S1, Table S3; Cai et al., 2016; Y. Chen et al., 2013; Sun et al., 2012; Zheng et al., 2018). Previous XKS studies likewise show NNW–SSE fast directions, consistent with our results (Figure S9c in Supporting Information S1).

Surface-wave tomography (Bao et al., 2020; Z. Zhang et al., 2023) shows that in the crust, fast axes align with major fault-zone strikes near the MCD array (Figures S10a and S10b in Supporting Information S1), although anisotropic strength differs between the two studies. In the lithospheric mantle, fast axes rotate to roughly E–W (Figure S10c in Supporting Information S1), nearly perpendicular to both fault strikes (NNW or NS) and southeastward asthenospheric flow (SSE, Z. Huang & Chevrot, 2021). This orthogonality may contribute to our relatively small mean XKS delay time (∼0.83 ± 0.18 s), which is lower than the global average (∼1.0 s) despite the intensively active tectonic deformation and anticipated mantle flow in southeast Tibet.

Anisotropy revealed by Pn tomography (Figure S11a in Supporting Information S1, Lü et al., 2017) shows dominant NNW–SSE/NS orientations across most of the study area, matching crustal surface-wave results and fault-zone strikes. In contrast, *P*-wave anisotropy at 120 km depth (Figure S11b in Supporting Information S1, Z. Huang et al., 2015) is mostly E–W, consistent with the ∼175 km surface-wave pattern (Figure S10c in Supporting Information S1). This approximate orthogonality with the fast directions from XKS splitting supports the interpretation of reduced XKS delay times in this region.

4.2. Implications on Mantle Flow

Numerous shear-wave splitting studies have shown that azimuthal anisotropy largely reflects lithospheric deformation and simple shear in the upper asthenosphere driven by lithosphere–asthenosphere relative motion (e.g., Conrad et al., 2007). Along the MCD array, the crustal thickness (Figure 4e), crustal anisotropy (Figure S9b

Figure 4. Spatial distribution of XKS shear-wave splitting parameters along the Middle ChuanDian (MCD) profile. Gray vertical lines are borders of four sub-blocks. (a) Topography along the profile. The black triangles are MCD array stations with more than 5 measurements, the gray triangles are stations with less than 5 measurements, and blue triangles are the permanent stations. (b) Number of non-null measurements. The scale at the left side corresponds to the number of measurements at the MCD array stations, while the scale at the right side corresponds to the number of measurements at the permanent stations. (c) Fast polarization direction (FPD). (d) Delay time (Delaytime). Red dashed line represents the average for all measurements while other colored dashed lines are averages for the four sub-areas. (e) Ps/P and Moho depth (dashed line, L. Li et al., 2024). (f) S velocity, in which LVZ means lower velocity zone while HVZ means higher velocity zone. The two LVZs are marked by black dashed lines and white circle are earthquakes with $M \geq 4$ (L. Li et al., 2024).

in Supporting Information S1), lithospheric deformation patterns (Figure S10 in Supporting Information S1), and lithospheric thickness (Figure 3a) all vary markedly. For example, A. Zhang et al. (2024) report lithospheric thickness increasing from approximately 100 km beneath the southwestern end of the array to about 160 km beneath its northeastern terminus (Figure 3a). If lithospheric deformation were the dominant control on seismic anisotropy, one would expect splitting times to increase gradually toward the northeast, which is absent. Instead, the uniformity of splitting parameters along the array points to an asthenospheric source, with local perturbations from major faults and tectonic boundaries (see next section).

Additional evidence for an asthenospheric origin comes from the azimuthal dependence of fast directions at certain permanent stations (Figure S6 in Supporting Information S1), where arrivals from the north deviate more strongly from a N–S alignment than arrivals from other directions. This behavior is consistent with a more eastward mantle flow north of the MCD array, that is, the apparent azimuthal variation is caused by piercing point dependence of the anisotropy structure, as recently reported (Jia et al., 2021) at stations located near the northeastern edge of the SCB. This piercing point dependence of seismic anisotropy is consistent with the observation that mantle flow beneath the interior Tibetan Plateau is predominantly eastward, transitioning toward a southerly direction near the eastern margin of the Plateau.

4.3. Fault Zone Related Seismic Anisotropy

Southeast Tibet is crisscrossed by several large-scale strike-slip faults, but their effect on XKS splitting has been difficult to isolate. Thanks to the dense MCD array, which transects these structures, we observe an abrupt reorientations of fast directions locally align with fault strikes, most prominently beneath the MBF and DLSF (Figure 4c). Moreover, delay times exhibit step-like changes that coincide with the ANHF–ZMHF, DLSF, and MBF fault traces (Figures 3c, 4a, and 4d), highlighting fault-zone–related anisotropy.

Under the assumption that major faults can produce ∼4% anisotropy (Barruol & Mainprice, 1993), we can estimate the depth extent of the fault zones, using (Silver & Chan, 1991):

$$A = \frac{\delta t * Vs}{d} \tag{1}$$

where A is the amplitude of seismic anisotropy (0.04), δt is the delay time contributed by the fault zone, Vs is shear-wave speed in km/s which is assumed to be 3.5 km/s, and d is the depth extent of the fault zone in km. Using a δt of 0.1 s beneath the ANHF-ZMHF and DLSF, and 0.3 s beneath the MBF (Figures 3 and 4), the resulting depth extent for the ANHF-ZMHF and DLSF is about 9 km, while the MBF may extend to ∼26 km. Because the Moho depth is ∼60 km beneath the ANHF-ZMHF and DLSF, and ∼40 km beneath the MBF (L. Li et al., 2024; Figure 4e), the results suggest that the ANHF-ZMHF and DLSF are limited in the upper crust, while the MBF extends into the mid-crust. However, these depth estimates carry substantial uncertainties, stemming from both the assumed anisotropy magnitude and the simplistic view of fault-zone uniformity.

Kaviani et al. (2011) demonstrated that topographic gradients across the Dead Sea Basin (DSB) correlate with pronounced variations in XKS delay times, which reach minima beneath the basin. Their synthetic models attribute these spatial patterns to the thick sedimentary fill and its low isotropic seismic velocities. We observe some along-profile variation in XKS splitting in our study (Figure 4d). Although topography does vary, it does so smoothly (Figure 4a), without the sharp contrasts seen at the DSB. We acknowledge that a basin effect may be present here, but extensive basins are uncommon in southeast Tibet, and the ∼10 km station spacing of the MCD array limits our ability to resolve small-scale basin influences. Future work using a much denser array will be needed to investigate any localized basin contributions more definitively.

5. Conclusions

We performed XKS shear-wave splitting analysis on 1,877 measurements obtained from the 2-year MCD temporary array and 13 years of observations at six permanent stations. Fast polarization directions consistently align NNW–SSE, indicating that southeastward-directed asthenospheric flow dominates the regional anisotropic signature. Spatial variations in delay times reveal pronounced increases adjacent to major fault systems. Localized rotations of fast directions toward fault strikes and step-like delay-time contrasts confirm a secondary, fault zone related contribution to the observed anisotropy. The estimated fault penetration depths of ∼9 km for the

Anninghe–Zemuhe and Daliangshan faults and ~26 km for the MBF. These results underscore the critical role of crustal discontinuities in modulating seismic anisotropy and introduce a quantitative framework for inferring fault-zone depth from splitting measurements. Our findings highlight the robustness of temporary dense arrays for high-resolution anisotropy studies, the existence and direction of asthenospheric flow beneath southeast Tibet, and the measurable imprint of fault structures on seismic anisotropy.

Data Availability Statement

Data of XKS splitting from MCD array and six permanent stations [Dataset] (Wu, 2025).

SplitLab: 2008 Release [Software] (Wüstefeld et al., 2008).

GMT: 2019 Release (Version 6) [Software] (Wessel et al., 2019).

Acknowledgments
We are thankful to Editor Prof. Daoyuan Sun, Associate Editor Prof. Germán A. Prieto, and two anonymous reviewers for their constructive and valuable feedbacks that improve this study significantly. We thank Drs. Greg Beroza and William L. Ellsworth (Stanford University), Yingcai Zheng (University of Houston), Fenglin Niu, Huajian Yao (University of Science and Technology, China), Xuewei Bao (Zhejiang University), Zhouchuan Huang (Nanjing University), Liang Zhao, Yan Lü, Chenglong Wu, and Xinai Zhao (Institute of Geology and Geophysics, Chinese Academy of Sciences), and Wei Li (China University of Geosciences), for their helpful suggestions. This study is supported by CAS Project for Young Scientists in Basic Research (YSBR-082), Strategy Priority Research Program (Category B) of Chinese Academy of Sciences (XDB0710000), and State Key Laboratory of Lithospheric and Environmental Coevolution (SKL-202305).

References

Bai, D., Unsworth, M. J., Meju, M. A., Ma, X., Teng, J., Kong, X., et al. (2010). Crustal deformation of the eastern Tibetan Plateau revealed by magnetotelluric imaging. *Nature Geoscience*, *3*(5), 358–362. https://doi.org/10.1038/ngeo830

Bao, X., Song, X., Eaton, D. W., Xu, Y., & Chen, H. (2020). Episodic lithospheric deformation in eastern Tibet inferred from seismic anisotropy. *Geophysical Research Letters*, *47*(3), e2019GL085721. https://doi.org/10.1029/2019GL085721

Barruol, G., & Mainprice, D. (1993). A quantitative evaluation of the contribution of crustal rocks to the shear-wave splitting of teleseismic SKS waves. *Physics of the Earth and Planetary Interiors*, *78*(3–4), 281–300. https://doi.org/10.1016/0031-9201(93)90161-2

Bowman, J. R., & Ando, M. (1987). Shear-wave splitting in the upper-mantle wedge above the Tonga subduction zone. *Geophysical Journal International*, *88*(1), 25–41. https://doi.org/10.1111/j.1365-246X.1987.tb01367.x

Cai, Y., Wu, J., Fang, L., Wang, W., & Yi, S. (2016). Crustal anisotropy and deformation of the southeastern margin of the Tibetan Plateau reveled by Pms splitting. *Journal of Asian Earth Sciences*, *121*, 120–126. https://doi.org/10.1016/j.jseaes.2016.02.005

Chen, A., Gao, Y., & Shi, Y. (2019). Seismic anisotropy and its variation in the upper crust beneath the Longmenshan Fault Zone. *Chinese Journal of Geophysics*, *62*(8), 2959–2981. https://doi.org/10.6038/cjg2019M0179

Chen, X., Li, Y., & Levin, V. (2018). Shear wave splitting beneath eastern North American continent: Evidence for a multilayered and laterally variable anisotropic structure. *Geochemistry, Geophysics, Geosystems*, *19*(8), 2857–2871. https://doi.org/10.1029/2018GC007646

Chen, Y., Zhang, Z., Sun, C., & José, B. (2013). Crustal anisotropy from Moho converted Ps wave splitting analysis and geodynamic implications beneath the eastern margin of Tibet and surrounding regions. *Gondwana Research*, *24*(3–4), 946–957. https://doi.org/10.1016/j.gr.2012.04.003

Clark, M. K., & Royden, L. H. (2000). Topographic ooze: Building the eastern margin of Tibet by lower crustal flow. *Geology*, *28*(8), 703–706. https://doi.org/10.1130/0091-7613(2000)28<703:TOBTEM>2.0.CO;2

Conrad, C. P., Behn, M. D., & Silver, P. G. (2007). Global mantle flow and the development of seismic anisotropy: Differences between the oceanic and continental upper mantle. *Journal of Geophysical Research*, *112*(B7), B07317. https://doi.org/10.1029/2006JB004608

Crampin, S. (1984). An introduction to wave propagation in anisotropic media. *Geophysical Journal International*, *76*(1), 17–28. https://doi.org/10.1111/j.1365-246X.1984.tb05018.x

Crampin, S., & Peacock, S. (2005). A review of shear-wave splitting in the compliant crack-critical anisotropic Earth. *Wave Motion*, *41*(1), 59–77. https://doi.org/10.1016/j.wavemoti.2004.05.006

Favier, N., & Chevrot, S. (2003). Sensitivity kernels for shear wave splitting in transverse isotropic media. *Geophysical Journal International*, *153*(1), 213–228. https://doi.org/10.1046/j.1365-246X.2003.01894.x

Hu, F., Wu, F., Ducea, M. N., Chapman, J. B., & Yang, L. (2022). Does large-scale crustal flow shape the eastern margin of the Tibetan Plateau? Insights from episodic magmatism of Gongga-Zheduo granitic massif. *Geophysical Research Letters*, *49*(12), e2022GL098756. https://doi.org/10.1029/2022GL098756

Huang, P., Gao, Y., & Wu, J. (2024). Crustal anisotropy beneath southeast Tibet revealed by Pms arrival times. *Terra Nova*, *36*(5), 315–326. https://doi.org/10.1111/ter.12714

Huang, Z., & Chevrot, S. (2021). Mantle dynamics in the SE Tibetan Plateau revealed by teleseismic shear-wave splitting analysis. *Physics of the Earth and Planetary Interiors*, *313*, 106687. https://doi.org/10.1016/j.pepi.2021.106687

Huang, Z., Zhao, D., & Wang, L. (2015). P wave tomography and anisotropy beneath southeast Asia: Insight into mantle dynamics. *Journal of Geophysical Research: Solid Earth*, *120*(7), 5154–5174. https://doi.org/10.1002/2015JB012098

Hubbard, J., & Shaw, J. H. (2009). Uplift of the Longmen Shan and Tibetan Plateau, and the 2008 Wenchuan (M = 7.9) earthquake. *Nature*, *458*(7235), 194–197. https://doi.org/10.1038/nature07837

Jia, Y., Liu, K. H., Kong, F., Liu, L., & Gao, S. S. (2021). A systematic investigation of piercing-point-dependent seismic azimuthal anisotropy. *Geophysical Journal International*, *227*(3), 1496–1511. https://doi.org/10.1093/gji/ggab285

Kaviani, A., Rümpker, G., Weber, M., & Asch, G. (2011). Short-scale variations of shear-wave splitting across the Dead Sea basin: Evidence for the effects of sedimentary fill. *Geophysical Research Letters*, *38*(4), L04308. https://doi.org/10.1029/2010GL046464

Li, L., Wang, X., Hou, G., Ling, Y., & Ai, Y. (2024). Two thin middle-crust low-velocity zones imaged in the Chuan-Dian region of southeastern Tibetan Plateau and their tectonic implications. *Science China Earth Sciences*, *67*(5), 1675–1686. https://doi.org/10.1007/s11430-023-1256-0

Li, W., Chen, Y., Liang, X., & Xu, Y. G. (2021). Lateral seismic anisotropy variations record interaction between Tibetan mantle flow and plume-strengthened Yangtze craton. *Journal of Geophysical Research: Solid Earth*, *126*(4), e2020JB020841. https://doi.org/10.1029/2020JB020841

Liu, H., & Niu, F. (2012). Estimating crustal seismic anisotropy with a joint analysis of radial and transverse receiver function data. *Geophysical Journal International*, *188*(1), 144–164. https://doi.org/10.1111/j.1365-246X.2011.05249.x

Liu, J., Wu, J., Wang, W., Fang, L., & Chang, K. (2020). Seismic anisotropy beneath the eastern margin of the Tibetan Plateau from SKS splitting observations. *Tectonophysics*, *785*, 228430. https://doi.org/10.1016/j.tecto.2020.228430

Long, M. D., & Silver, P. G. (2009). Shear wave splitting and mantle anisotropy: Measurements, interpretations, and new directions. *Surveys in Geophysics*, *30*(4–5), 407–461. https://doi.org/10.1007/s10712-009-9075-1

Lü, Y., Ni, S., Chen, L., & Chen, Q. (2017). Pn tomography with Moho depth correction from eastern Europe to western China. *Journal of Geophysical Research: Solid Earth*, *122*(2), 1284–1301. https://doi.org/10.1002/2016JB013052

McNamara, D. E., Owens, T. J., Silver, P. G., & Wu, F. T. (1994). Shear wave anisotropy beneath the Tibetan Plateau. *Journal of Geophysical Research*, *99*(B7), 13655–13665. https://doi.org/10.1029/93JB03406

Montagner, J. P., & Nataf, H. C. (1986). A simple method for inverting the azimuthal anisotropy of surface waves. *Journal of Geophysical Research*, *91*(B1), 511–520. https://doi.org/10.1029/JB091iB01p00511

Restivo, A., & Helffrich, G. (1999). Teleseismic shear wave splitting measurements in noisy environments. *Geophysical Journal International*, *137*(3), 821–830. https://doi.org/10.1046/j.1365-246x.1999.00845.x

Rümpker, G., Kaviani, A., & Latifi, K. (2014). Ps-splitting analysis for multilayered anisotropic media by azimuthal stacking and layer stripping. *Geophysical Journal International*, *199*(1), 146–163. https://doi.org/10.1093/gji/ggu154

Savage, M. K. (1999). Seismic anisotropy and mantle deformation: What have we learned from shear wave splitting? *Reviews of Geophysics*, *37*(1), 65–106. https://doi.org/10.1029/98RG02075

Silver, P. G. (1996). Seismic anisotropy beneath the continents: Probing the depths of geology. *Annual Review of Earth and Planetary Sciences*, *24*(1), 385–432. https://doi.org/10.1146/annurev.earth.24.1.385

Silver, P. G., & Chan, W. W. (1991). Shear wave splitting and subcontinental mantle deformation. *Journal of Geophysical Research*, *96*(B10), 16429–16454. https://doi.org/10.1029/91JB00899

Sun, Y., Niu, F., Liu, H., Chen, Y., & Liu, J. (2012). Crustal structure and deformation of the SE Tibetan Plateau revealed by receiver function data. *Earth and Planetary Science Letters*, *349–350*, 186–197. https://doi.org/10.1016/j.epsl.2012.07.007

Tapponnier, P., Xu, Z., Roger, F., Meyer, B., Arnaud, N., Wittlinger, G., & Jingsui, Y. (2001). Oblique stepwise rise and growth of the Tibet Plateau. *Science*, *294*(5547), 1671–1677. https://doi.org/10.1126/science.105978

Teanby, N. A., Kendall, J. M., & Van der Baan, M. (2004). Automation of shear-wave splitting measurements using cluster analysis. *Bulletin of the Seismological Society of America*, *94*(2), 453–463. https://doi.org/10.1785/0120030123

Vinnik, L. P., Kind, R., Kosarev, G. L., & Makeyeva, L. I. (1989). Azimuthal anisotropy in the lithosphere from observations of long-period S-waves. *Geophysical Journal International*, *99*(3), 549–559. https://doi.org/10.1111/j.1365-246X.1989.tb02039.x

Wang, C. Y., Flesch, L. M., Silver, P. G., Chang, L. J., & Chan, W. W. (2008). Evidence for mechanically coupled lithosphere in central Asia and resulting implications. *Geology*, *36*(5), 363–366. https://doi.org/10.1130/G24450A.1

Wang, J., Huang, X., Zhao, D., & Yao, Z. (2019). Seismic anisotropy evidence for ductile deformation of the forearc lithospheric mantle in subduction zones. *Journal of Geophysical Research: Solid Earth*, *124*(7), 7013–7027. https://doi.org/10.1029/2018JB016912

Wessel, P., Luis, J. F., Uieda, L. A., Scharroo, R., Wobbe, F., Smith, W. H., & Tian, D. (2019). GMT: 2019 release (version 6) [Software]. Retrieved from https://www.generic-mapping-tools.org/download/

Wu, J. (2025). Data of XKS splitting from MCD array and six permanent stations [Dataset]. *WDC (World Data Center) for Geophysics, Beijing*. https://doi.org/10.12197/2025GA009

Wu, J., Zhang, Z., Kong, F., Yang, B. B., Yu, Y., Liu, K. H., & Gao, S. S. (2015). Complex seismic anisotropy beneath western Tibet and its geodynamic implications. *Earth and Planetary Science Letters*, *413*, 167–175. https://doi.org/10.1016/j.epsl.2015.01.002

Wüstefeld, A., Bokelmann, G., Zaroli, C., & Barruol, G. (2008). SplitLab: 2008 release [Software]. Retrieved from https://splitting.gm.univ-montp2.fr

Wüstefeld, A., & Bokelmann, G. (2007). Null detection in shear-wave splitting measurements. *Bulletin of the Seismological Society of America*, *97*(4), 1204–1211. https://doi.org/10.1785/0120060190

Yang, F., Li, J., Chen, S., Chen, Y., Li, L., & Ai, Y. (2023). Intracontinental lithospheric delamination: Constraints from imaging the mantle transition zone beneath the southwestern part of the Sichuan Basin. *Science China Earth Sciences*, *66*(10), 2340–2352. https://doi.org/10.1007/s11430-022-1129-9

Yang, Y., Liang, C., Fang, L., Su, J., & Hua, Q. (2018). A comprehensive analysis on the stress field and seismic anisotropy in eastern Tibet. *Tectonics*, *37*(6), 1648–1657. https://doi.org/10.1029/2018TC005011

Yin, A., & Harrison, T. M. (2000). Geologic evolution of the Himalayan-Tibetan Orogen. *Annual Review of Earth and Planetary Sciences*, *28*(1), 211–280. https://doi.org/10.1146/annurev.earth.28.1.211

Zhang, A., Guo, Z., Afonso, J. C., Shellnutt, J. G., & Yang, Y. (2024). Mantle plume-lithosphere interactions beneath the Emeishan large igneous province. *Geophysical Research Letters*, *51*(2), e2023GL106973. https://doi.org/10.1029/2023GL106973

Zhang, S., & Karato, S. I. (1995). Lattice preferred orientation of olivine aggregates deformed in simple shear. *Nature*, *375*(6534), 774–777. https://doi.org/10.1038/375774a0

Zhang, Y., & Gao, Y. (2017). The characteristics of crustal shear-wave splitting in North-South seismic zone revealed by near field recordings of two observation periods of ChinArray. *Chinese Journal of Geophysics*, *60*(6), 2181–2199. https://doi.org/10.6038/cjg20170613

Zhang, Z., Feng, J., & Yao, H. (2023). 3-D azimuthal anisotropy structure reveals different deformation modes of the crust and upper mantle in the southeastern Tibetan Plateau. *Frontiers in Earth Science*, *11*, 1095609. https://doi.org/10.3389/feart.2023.1095609

Zhao, D., Wang, J., Huang, Z., Liu, X., & Wang, Z. (2023). Seismic anisotropy and geodynamics of the East Japan subduction zone. *Journal of Geodynamics*, *156*, 101975. https://doi.org/10.1016/j.jog.2023.101975

Zhao, L., Zhao, M., & Lü, G. (2014). Upper mantle seismic anisotropy beneath a convergent boundary: SKS waveform modeling in central Tibet. *Science China Earth Sciences*, *57*(4), 759–776. https://doi.org/10.1007/s11430-014-4826-3

Zhao, X., & Wu, J. (2024). Major methods of seismic anisotropy. *Earthquake Research Advances*, *4*(3), 100295. https://doi.org/10.1016/j.eqrea.2024.100295

Zheng, T., Ding, Z., Ning, J., Chang, L., Wang, X., Kong, F., et al. (2018). Crustal azimuthal anisotropy beneath the southeastern Tibetan Plateau and its geodynamic implications. *Journal of Geophysical Research: Solid Earth*, *123*(11), 9733–9749. https://doi.org/10.1029/2018JB015995